PHYSICAL REVIEW B **77**, 205437 (2008)

Elastic properties and pressure-induced structural transitions of single-walled carbon nanotubes

K. M. Liew and Yuzhou Sun
Department of Building and Construction, City University of Hong Kong, Kowloon, Hong Kong

(Received 20 November 2007; revised manuscript received 10 February 2008; published 30 May 2008)

The mechanical properties and pressure-induced structural transitions of single-walled carbon nanotubes (SWCNTs) are studied in this paper in the theoretical scheme of the higher-order gradient continuum. Both the first- and second-order deformation gradients are involved in the approximation of the deformations of microscale lattice vectors, and the continuum elastic potential is obtained by equating the deformation energy of a representative cell with that of an equivalent volume of the continuum, and thus, the established continuum constitutive model is more reasonable. By setting an appropriate equation as the deformation map from a graphite sheet to an initial undeformed SWCNT, the elastic constants of SWCNTs are obtained by minimizing the energy of a representative cell. The response of SWCNTs under axis-symmetrical loadings can also be obtained by changing the values of the set geometrical parameters. Based on the derived constitutive model, a computational method is developed to study the response of SWCNTs under hydrostatic pressure.

DOI: 10.1103/PhysRevB.77.205437 PACS number(s): 62.25.−g, 68.65.−k, 61.46.Fg

I. INTRODUCTION

The discovery of carbon nanotubes (CNTs) in 1991 by Iijima[1] sparked a revolution in chemical physics and materials science. Much research has been carried out on this new form of structure due to its outstanding physical, mechanical, and electrical properties. CNTs are generally modeled and studied through atomistic modeling approaches.[2–6] However, they consume a tremendous amount of computational time and resources, and their study is limited to a very small size. Some equivalent continuum models have been developed[7–14] and have proved to be very efficient from the computational point of view. These continuum-based methods are much faster than molecular simulations for systems of engineering interest, which makes them attractive. Govindjee and Sackman[7] adopted the Euler beam theory to study the elastic properties of CNTs and showed the dependency of the elastic properties at nanoscale dimensions. Ru[9] treated a single-walled carbon nanotubes (SWCNT) as a single-layer elastic shell with an effective bending stiffness and studied the buckling behaviors of CNTs. Li and Chou[11] developed a molecular structural mechanics approach to study the elastic properties of SWCNTs. He *et al.*[12] developed a continuum model to account for van der Waals interaction between the different walls of CNTs. Wang and Hu[13] and Liew *et al.*[14] used the strain gradient to model the dispersion of the flexural and longitudinal waves in CNTs.

Another continuum modeling approach is to construct the finite deformation continuum theory through the Cauchy–Born rule,[15,16] in which the constitutive model is written in terms of the underlying atomistic model. The first use of this method on the nanoscale emerged from the quasicontinuum method for two-dimensional problems.[16–18] Later, Zhang *et al.*[19,20] extended the approach to CNTs and studied the axial Young's modulus and fracture nucleation. However, as Arroyo and Belytschko[21,22] indicated, the direct application of this rule to CNTs is insufficient and inaccurate because a CNT is essentially a curved crystalline sheet of an atom thickness, and the curvature effect has to be accounted for. In Refs. 21 and 22, an exponential Cauchy–Born rule for the finite deformation membrane and CNTs was formulated, with the derived hyperelastic potential being dependent on the stretch and the curvature of the surface. In studying the planar crystals, Sunyk and Steinmann[23] pointed out that the Cauchy–Born rule requires sufficiently homogeneous deformations of the underlying crystal and suggested the application of the higher-order gradient in the continuum modeling of the inhomogeneous deformations. Guo *et al.*[24] and Wang *et al.*[25] recently extended the standard Cauchy–Born rule by considering the effect of the second-order gradient and proposed a higher-order Cauchy–Born rule for SWCNTs

The present work follows the contributions of Refs. 23–25 and investigates the elastic properties and hydrostatic pressure-induced structural transition of SWCNTs. The theoretical framework is similar to the higher-order gradient continuum theory of linear elasticity,[26] in which the strain energy density is a function of the first- and second-order deformation gradients. By approximating the deformations of the bond vectors with the higher-order Cauchy–Born rule,[25] the continuum elastic potential can be obtained by equating the deformation energy of a representative cell to that of an equivalent volume of the continuum. The resulting continuum constitutive model depends only on the interatomic interactions, with no additional phenomenological input. The boundary value problems can be solved in the scheme of the higher-order continuum theory. In the present investigation, the map from a planar graphite sheet to an undeformed SWCNT is written in an analytical form with three geometrical parameters that correspond, respectively, to the axial and circumferential stretches and the twisting angle. By minimizing the energy of the cell structure, the structural properties and the elastic constants (Young's moduli, shear moduli, and Poisson's ratio) of SWCNTs can be obtained. The set mapping equations also describe any axis-symmetrical deformations of SWCNTs, and thus, the response of SWCNTs under axis-symmetrical loadings can be computed. The computational results show that the involvement of the second gradient can provide an accurate analysis of CNTs.

The response of CNTs under hydrostatic pressure is currently a topic of interest. Investigations have found that a

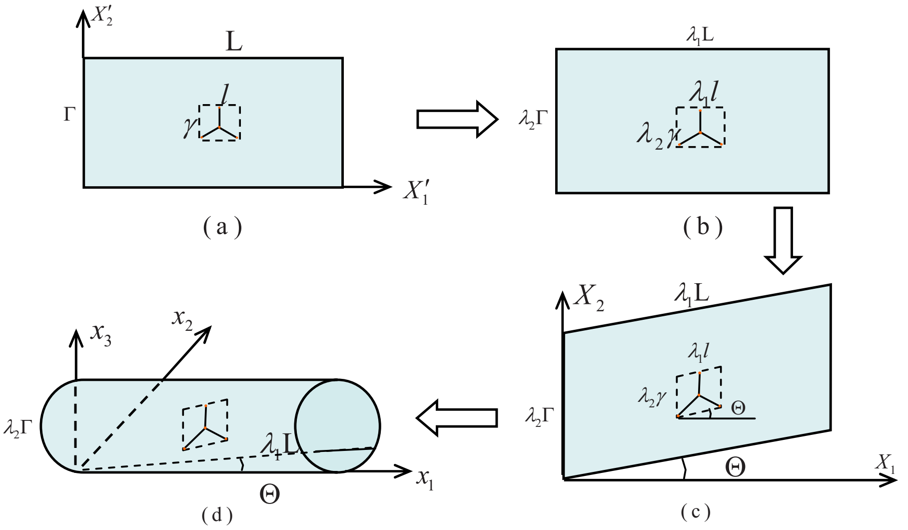

FIG. 1. (Color online) SWCNT formed by rolling an equilibrium graphite sheet into a cylindrical shape through three steps; the change of the representative cell is also depicted.

structural transition occurs under a higher hydrostatic pressure, and that this largely changes the mechanical and electrical properties of CNTs.[27–29] Currently, most of the work to simulate the hydrostatic pressure response is based on molecular dynamics. Using the hyperelastic constitutive model derived from the higher-order Cauchy–Born rule, we develop a computational method to study the structural transition of SWCNTs. The SWCNT is considered as a ring, and the strain energy of the CNTs can be written in terms of the radial displacement of the ring and the two geometrical parameters that correspond to the axial and twisting deformations. The mesh-free method[30–35] is used to determine a stable configuration in the scheme of the higher-order gradient continuum.

Empirical potentials are generally used in the analysis of CNTs to describe the interatomic interactions. A widely used bond-order potential is the Tersoff–Brenner potential.[36,37] This potential is employed in the present work, and the second parameter set[37] is used in our computations.

II. HIGHER-ORDER GRADIENT CONTINUUM AND CONSTITUTIVE EQUATIONS

An undeformed SWCNT can be viewed as being formed by rolling up a graphite sheet into a cylindrical shape (Fig. 1). This rolling process, however, is not a simple rigid transformation, and the microstructure will readjust to attain the minimum system energy during the rolling. Here, we decompose this transformation into three steps, as shown in Fig. 1. Figure 1(a) is an initial equilibrium graphite sheet with length L and width Γ, and it is rolled up along the axis X_2'. In Fig. 1(b), the parameters λ_1 and λ_2, respectively, correspond to the uniform longitudinal and circumferential stretches; thus, $\lambda_2\Gamma$ is equal to the perimeter of the tube. The angle Θ in Fig. 1(c) corresponds to the skew angle of any surface longitudinal line in Fig. 1(d). The deformation map from Fig. 1(a) to Fig. 1(d) $[\mathbf{x}=\mathbf{x}(\mathbf{X}')]$ can be written as

$$x_1 = \lambda_1 X_1', \tag{1a}$$

$$x_2 = \frac{\lambda_2\Gamma}{2\pi}\sin\left(\frac{X_2'}{\Gamma}2\pi + \Phi\lambda_1 X_1'\right), \tag{1b}$$

$$x_3 = \frac{\lambda_2\Gamma}{2\pi} - \frac{\lambda_2\Gamma}{2\pi}\cos\left(\frac{X_2'}{\Gamma}2\pi + \Phi\lambda_1 X_1'\right), \tag{1c}$$

where Φ is the twisting angle per unit length $\Phi=\Theta/R$, and R is the radius of the tube). For any vector $\mathbf{R}$ emanating from point $\mathbf{X}'$ in the reference configuration, it is mapped to $\mathbf{r} = \mathbf{x}(\mathbf{X}'+\mathbf{R})-\mathbf{x}(\mathbf{X}')$.

Expanding $\mathbf{x}(\mathbf{X}'+\mathbf{R})$ in a Taylor series about $\mathbf{X}'$ and retaining up to the second-order term, we have the approximation

$$\mathbf{r} \approx \mathbf{F}(\mathbf{X}')\cdot\mathbf{R} + \frac{1}{2}\mathbf{G}(\mathbf{X}'):(\mathbf{R}\otimes\mathbf{R}), \tag{2}$$

where $\mathbf{F}=\nabla\mathbf{x}(\mathbf{X}')$ (rank-2 tensor) and $\mathbf{G}=\nabla\mathbf{F}(\mathbf{X}')$ (rank-3 tensor) are the first- and second-order deformation gradients, respectively. In the conventional Cauchy–Born rule,[15–20] the deformation is approximated only with $\mathbf{F}(\mathbf{X}')\cdot\mathbf{R}$. Equation (2) involves the effect of the second-order deformation gradient, and thus, the approximation is greatly enhanced. This improvement can be seen from Fig. 2. Maps (1a)–(1c) precisely transform the vector $\mathbf{R}$ to a curved line segment (the dot line in Fig. 2) on the surface of the tube. In Fig. 2, $\mathbf{r}'$ denotes the spatial vector that connects the two end points of this curved line segment, and it corresponds to the orientation of the deformed bond vector since a bond is essentially

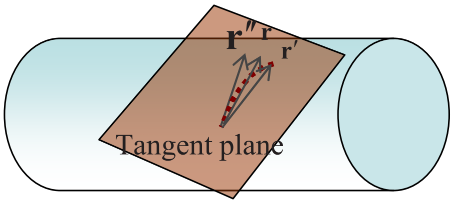

FIG. 2. (Color online) $\mathbf{F}(\mathbf{X}')\cdot\mathbf{R}$ maps the vector $\mathbf{R}$ onto the tangent plane as $\mathbf{r}''$; the enhanced term $\mathbf{G}(\mathbf{X}'):(\mathbf{R}\otimes\mathbf{R})/2$ pulls $\mathbf{r}''$ to $\mathbf{r}$ that is closer to the real case.

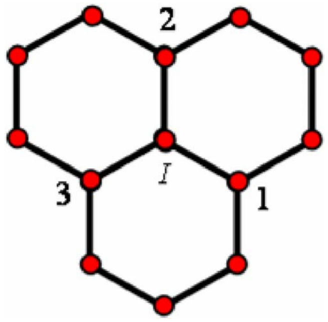

FIG. 3. (Color online) Representative cell composed of bonds $I-J(J=1,2,3)$.

a chord that is embedded into this surface. However, $\mathbf{F}(\mathbf{X}')\cdot\mathbf{R}$ only maps the vector $\mathbf{R}$ onto the tangent plane that passes through the emanating point (see the vector $\mathbf{r}''$ in Fig. 2). Equation (2) maps $\mathbf{R}$ to $\mathbf{r}$ that is closer to the actual case. The term $\mathbf{G}(\mathbf{X}'):(\mathbf{R}\otimes\mathbf{R})/2$ describes the difference between the vectors $\mathbf{r}$ and $\mathbf{r}''$. In particular, this term also describes the effect of the bending stiffness, which results in a more reasonable physical approximation.

In the higher-order gradient continuum,[23–26] the strain energy density W_0 is a function of the deformation gradients $\mathbf{F}$ and $\mathbf{G}$. The first Piola–Kirchhoff stress tensor $\mathbf{P}$ and the higher-order stress tensor $\mathbf{Q}$ are denoted as

$$\mathbf{P}=\frac{\partial W_0(\mathbf{F},\mathbf{G})}{\partial\mathbf{F}},\quad \mathbf{Q}=\frac{\partial W_0(\mathbf{F},\mathbf{G})}{\partial\mathbf{G}}. \tag{3}$$

To evaluate the strain energy density at a point, a cell structure is imaged at this point, as shown in Fig. 1. A magnified representative cell is shown in Fig. 3, in which the atom I is connected to bonds $I-J$ $(J=1,2,3)$. From Eq. (2), the deformation of the bond vectors can be approximated as

$$\mathbf{r}_{IJ}=\mathbf{F}\cdot(\mathbf{R}_{IJ}+\boldsymbol{\eta})+\mathbf{G}:[(\mathbf{R}_{IJ}+\boldsymbol{\eta})\otimes(\mathbf{R}_{IJ}+\boldsymbol{\eta})]/2, \tag{4}$$

where $\mathbf{R}_{IJ}$ and $\mathbf{r}_{IJ}$ denote the undeformed and deformed bond vectors, respectively. Moreover, an inner shift vector $\boldsymbol{\eta}=(\eta_1,\eta_2)$ has been added to the undeformed bond vector due to the noncentrosymmetry of the atomic structure.[16,19–22]

The strain energy density at this point can be calculated as

$$W_0(\mathbf{F},\mathbf{G})=\frac{V_0}{\Omega_I},$$

$$V_0=\frac{1}{2}\sum_{J=1}^{3}V_{IJ}(\mathbf{r}_{I1},\mathbf{r}_{I2},\mathbf{r}_{I3})=V_0[\mathbf{F},\mathbf{G},\boldsymbol{\eta}(\mathbf{F},\mathbf{G})], \tag{5}$$

where V_0 denotes the energy of atom I, Ω_I is the average area per atom in the reference configuration, and V_{IJ} is the Tersoff–Brenner potential.[36,37] It is noted that the inner shift is a function of $\mathbf{F}$ and $\mathbf{G}$, and the minimization of the atom energy often requires $\partial V_0/\partial\boldsymbol{\eta}=0$.

The tangential modulus can be obtained as

$$\mathbf{M}_{\mathbf{FF}}=\frac{\partial^2 W_0}{\partial\mathbf{F}\otimes\partial\mathbf{F}},\quad \mathbf{M}_{\mathbf{FG}}=\frac{\partial^2 W_0}{\partial\mathbf{F}\otimes\partial\mathbf{G}},$$

TABLE I. Optimization values for λ_1, λ_2, and Θ.

Type of SWCNT	λ_1	λ_2	Θ (°)
(9,6) chiral	1.00100	0.99411	0.08554
(5,5) armchair	1.00307	0.98606	0
(10,0) zigzag	0.99820	0.99346	0

$$\mathbf{M}_{\mathbf{GF}}=\frac{\partial^2 W_0}{\partial\mathbf{G}\otimes\partial\mathbf{F}},\quad \mathbf{M}_{\mathbf{GG}}=\frac{\partial^2 W_0}{\partial\mathbf{G}\otimes\partial\mathbf{G}}. \tag{6}$$

In the calculation of the tangential modulus, we should not ignore the contribution of the inner shift vector. For example, $\mathbf{M}_{\mathbf{FF}}$ is not equal to $\partial^2 V_0/\Omega_0\partial\mathbf{F}\otimes\partial\mathbf{F}$, and it should be calculated as

$$\mathbf{M}_{\mathbf{FF}}=\frac{\partial^2 W_0}{\Omega_0\,\partial\mathbf{F}\otimes\partial\mathbf{F}}=\frac{\partial^2 V_0}{\Omega_0\,\partial\mathbf{F}\otimes\partial\mathbf{F}}+\frac{\partial^2 V_0}{\Omega_0\,\partial\mathbf{F}\otimes\partial\boldsymbol{\eta}}\frac{\partial\boldsymbol{\eta}_0}{\partial\mathbf{F}}. \tag{7}$$

III. STRUCTURAL AND ELASTIC PROPERTIES OF SINGLE-WALLED CARBON NANOTUBES

The parameters λ_1, λ_2, Θ, η_1, and η_2 in Sec II can be obtained by minimizing the atom energy V_0 that is equivalent to

$$\frac{\partial V_I}{\partial\lambda_1}=\frac{\partial V_I}{\partial\lambda_2}=\frac{\partial V_I}{\partial\Phi}=\frac{\partial V_I}{\partial\eta_1}=\frac{\partial V_I}{\partial\eta_2}=0. \tag{8}$$

Equation (8) can be solved with an optimization approach, such as the conjugate gradient method.[38] Here, we use Newton's method,[38] in which the first- and second-order derivatives of V_0 with respect to these parameters are required at each iteration step.

A. Structural properties

With the solution of Eq. (8), the structural properties of the initial undeformed CNTs can be determined. Here, the second parameter set for the Tersoff–Brenner potential is adopted.[37] In the computation, we need to present a value as the initial bond length in the reference graphite sheet [Fig. 1(a)]. Essentially, we can choose any number as the initial bond length, and the choice of this initial value has no effect on the final optimized results. Moreover, by setting a very large tube radius, we can obtain the bond length in the initial equilibrium graphite sheet. For the second parameter set of the Tersoff–Brenner potential, our computation indicates that the bond length in the initial equilibrium graphite sheet is 0.14 507 nm. In the future calculation, we will use 0.14 507 nm as the initial value of the bond length in the reference configuration. With this choice, the evaluated values of λ_1, λ_2, and Θ have a clear physical significance, they are, respectively, the axial and circumferential stretches and twisting angle of the tube relative to the initial equilibrium graphite sheet. Table I shows the evaluated values of λ_1, λ_2, and Θ for the chiral (9,6), armchair (5,5), and zigzag (10,0)

TABLE II. Bond lengths, tube radius, and atom energy in the undeformed SWCNT.

Type of SWCNT	r_1 (nm)	r_2 (nm)	r_3 (nm)	R (nm)	V (eV)
(9,6) chiral	0.14520	0.14516	0.14533	0.51986	–7.33606
(5,5) armchair	0.14567	0.14532	0.14532	0.34150	–7.28637
(10,0) zigza	0.14518	0.14544	0.14544	0.39729	–7.30785

CNTs. It is worth noting that a nonzero twisting angle Θ occurs for the chiral CNT, whereas $\Theta=0$ for the armchair and zigzag CNTs. The evaluated bond lengths and tube radius are listed in Table II, along with the calculated atom energy. These results display excellent agreement with those of Jiang *et al.*[39] It is shown that the involvement of the second-order deformation gradient can provide an accurate analysis for CNTs.

B. Elasticity properties

A SWCNT can be viewed as a hollow cylinder of only one-atom thickness. The present model does not actually involve the thickness concept, and W_0 means the energy per unit area on the surface. For convenience of comparison only, we introduce a volume energy density $\hat{W}_0=W_0/t$, with t as the thickness (it is chosen as 0.334 nm, which is used in most of the literature).

Because λ_1 and λ_2 correspond, respectively, to the uniform longitudinal and circumferential stretches, the axial and circumferential strains are

$$\varepsilon_1=\lambda_1-1, \quad \varepsilon_\theta=\lambda_2-1. \tag{9}$$

The axial and circumferential stresses can be calculated as

$$\sigma_1=\frac{\partial \hat{W}_0}{\partial \varepsilon_1}=\frac{\partial \hat{W}_0}{\partial \lambda_1}, \quad \sigma_\theta=\frac{\partial \hat{W}_0}{\partial \varepsilon_\theta}=\frac{\partial \hat{W}_0}{\partial \lambda_2}. \tag{10}$$

In the case of hydrostatic pressure, CNTs deform uniformly along the circumference. The radial strains of the CNTs equal the circumferential strains, i.e., $\varepsilon_r=\varepsilon_\theta$. Moreover, the hydrostatic pressure p has a relationship with σ_θ as

$$p2R=\sigma_\theta 2t. \tag{11}$$

The axial and circumference Young's moduli can be obtained as

$$E_1=\frac{\partial^2 \hat{W}_0}{\partial \lambda_1^2}-\frac{\dfrac{\partial^2 \hat{W}_0}{\partial \lambda_1\,\partial \lambda_2}}{\dfrac{\partial^2 \hat{W}_0}{\partial \lambda_2^2}}, \quad E_\theta=\frac{\partial^2 \hat{W}_0}{\partial \lambda_2^2}-\frac{\dfrac{\partial^2 \hat{W}_0}{\partial \lambda_2\,\partial \lambda_1}}{\dfrac{\partial^2 \hat{W}_0}{\partial \lambda_1^2}}. \tag{12}$$

Using Eq. (11), the radial Young's modulus can be calculated as

$$E_r=E_\theta t/R. \tag{13}$$

Poisson's ratios are

$$v_{1\theta}=v_{1r}=\frac{\dfrac{\partial^2 \hat{W}_0}{\partial \lambda_2\,\partial \lambda_1}}{\dfrac{\partial^2 \hat{W}_0}{\partial \lambda_1\,\partial \lambda_1}}, \quad v_{\theta 1}=v_{r1}=\frac{\dfrac{\partial^2 \hat{W}_0}{\partial \lambda_1\,\partial \lambda_2}}{\dfrac{\partial^2 \hat{W}_0}{\partial \lambda_2\,\partial \lambda_2}}. \tag{14}$$

Moreover, we have the relationship

$$\frac{v_{1\theta}}{E_1}=\frac{v_{1r}}{E_1}=\frac{v_{\theta 1}}{E_\theta}=\frac{v_{r1}}{E_\theta}. \tag{15}$$

The angle Θ also has an obvious physical meaning, and it equals the shear strain $\gamma_{1\theta}$ at the surface. So, the shear stress at the cross section can be calculated as

$$\tau_{1\theta}=\frac{\partial \hat{W}_0}{\partial \Theta}=\frac{R\,\partial \hat{W}_0}{\partial \Phi}. \tag{16}$$

The shear modulus can be obtained as

$$G=\frac{\partial^2 \hat{W}_0}{\partial \Theta^2}=\frac{R^2 \partial^2 \hat{W}_0}{\partial \Phi^2}. \tag{17}$$

Similar to the way we calculate the tangential modulus, the contribution of the inner shift should be involved when we calculate the above elastic constants. Young's moduli and Poisson's ratios of CNTs are the values of Eqs. (12)–(17) at the initial equilibrium state of the CNTs.

Computations have been carried out for different types of CNTs. In the results analysis, we use $(3n,2n)$ CNTs as an example to illustrate the properties of chiral CNTs. In all of the calculations, the first- and second-order derivatives are exactly computed. Figure 4 shows the variation of the axial and circumferential Young's moduli with the tube radius. With an increasing tube radius, the axial and circumferential Young's moduli trend to the same constant that corresponds to Young's modulus of the graphite sheet. The present estimated value is 0.7049 TPa, which is very close to that predicted by Arroyo and Belytschko.[21] When the tube radius is larger than 0.5 nm, the moduli are very close to those of the graphite sheet, and the maximum difference is less than 2%. Moreover, we also notice a special phenomenon: the axial and circumferential Young's moduli of the CNTs are generally less than those of the graphite sheet, but the circumferential Young's moduli of the zigzag CNTs are slightly larger than those of the graphite sheet. This indicates that the chirality of CNTs has an effect on their properties, but this effect is very slight when the tube radius is larger than 0.5 nm. Plotted in Fig. 5 is the radial Young's modulus versus the tube radius. The radial Young's modulus has a large dependence on the tube radius because it is equal to the cir-

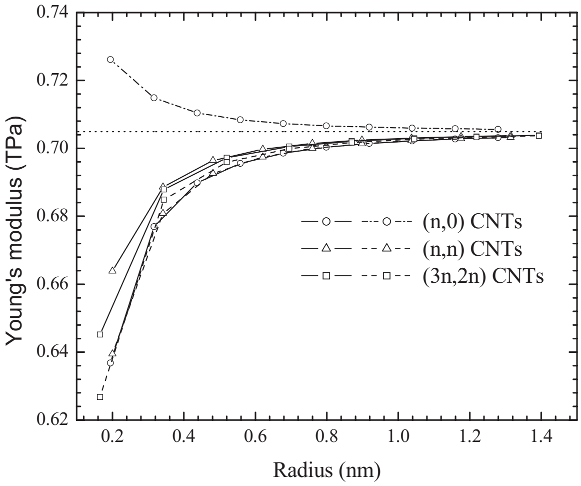

FIG. 4. Axial and circumferential Young's moduli versus tube radius for $(n,0)$, (n,n), and $(3n,2n)$ CNTs: the solid line for axial Young's modulus and the dashed line for circumferential Young's modulus.

cumferential Young's modulus divided by the tube radius. Figure 6 shows the variation of Poisson's ratio $\upsilon_{\theta 1}$ with the tube radius. Similar to the axial and circumferential Young's moduli, $\upsilon_{\theta 1}$ trends to Poisson's ratio of the graphite sheet (the present estimated value is 0.4123). When the tube radius is larger than 0.5 nm, Poisson's ratio is very close to 0.4123. Figure 7 shows the dependence of the shear modulus on the tube radius. When the tube radius is larger than 0.5 nm, the shear modulus is very close to that of the graphite sheet. The present estimated shear modulus of the graphite sheet is 0.25 TPa. In conclusion, the elastic properties of CNTs have a dependence on the chirality and the tube radius, but when the tube radius is larger than 0.5 nm, the axial and circumferential Young's moduli, Poisson's ratio, and shear modulus are pretty close to those of the graphite sheet. Therefore, CNTs can be viewed as a curved surface, on which the elastic properties at the tangent direct are almost the same with the graphite sheet.

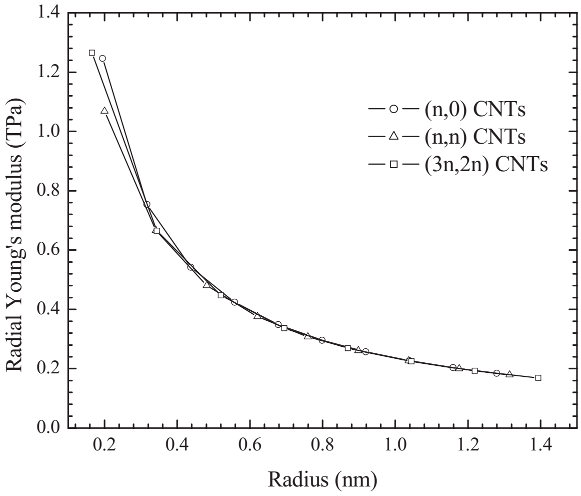

FIG. 5. Radial Young's modulus versus tube radius for $(n,0)$, (n,n), and $(3n,2n)$ CNTs.

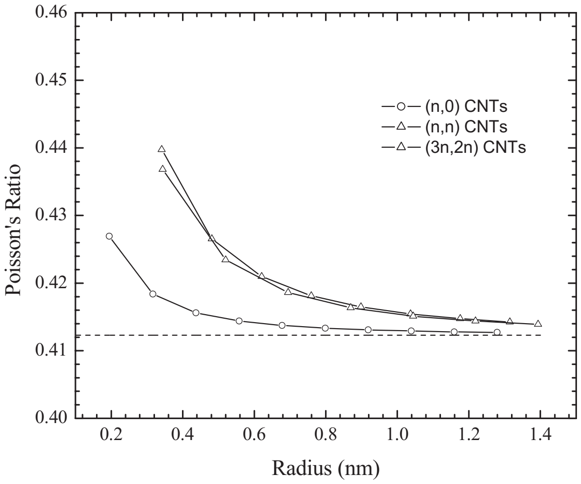

FIG. 6. Poisson's ratio versus tube radius for $(n,0)$, (n,n), and $(3n,2n)$ CNTs.

C. Pressure-radial strain curve

The above method can be viewed as an analytical-numerical method, in which the first- and second-order derivatives of the strain energy density are calculated exactly, and Newton's method is used only to determine the minimum point of energy. Moreover, by varying the values of λ_1, λ_2, and Θ and then minimizing the energy density, we can calculate the mechanical response of CNTs under axial tension or compression (varying λ_1), hydrostatic pressure (varying λ_2), and twisting (varying Θ). This method can also be used to study the interaction of different loading conditions, for example, the twisting behavior of different chiralities of CNTs under axial or radial compression. Here, we only offer the pressure-radial strain curve of SWCNTs under hydrostatic pressure. For a given λ_2 (that corresponds to a radial compression), the energy minimization will result in λ_1 and Θ, and then, the hydrostatic pressure can be calculated as $p=\partial W_0 / R \partial \lambda_2$. By varying λ_2, the curve of the hydrostatic pressure versus the radial strain $(\lambda_2 - 1)$ can be obtained. Plotted in Fig. 8 is the pressure-radial strain curve of a

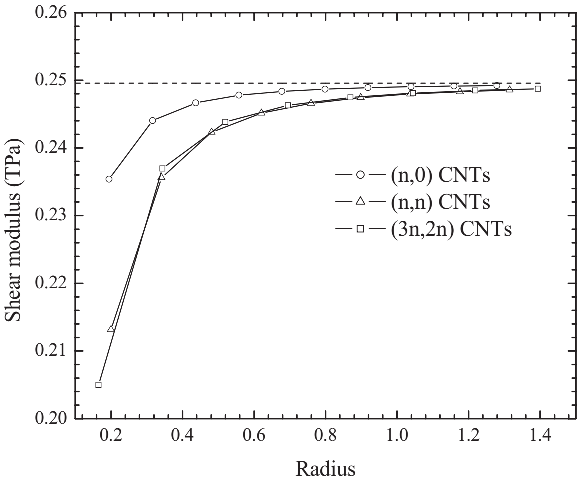

FIG. 7. Shear Young's modulus versus tube radius for $(n,0)$, (n,n), and $(3n,2n)$ CNTs.

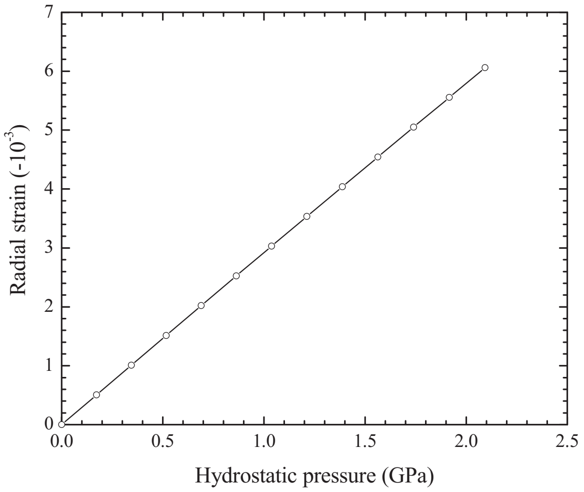

FIG. 8. Hydrostatic pressure-radial strain relationship curve that is obtained with an analytical-numerical method.

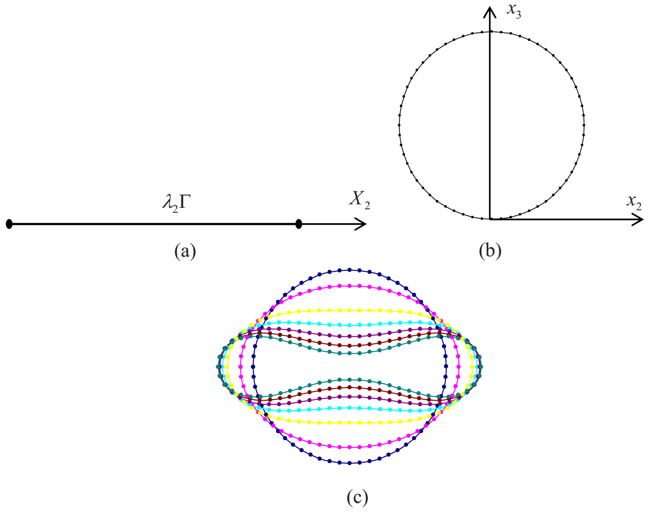

FIG. 9. (Color online) (a) SWCNT simplified as an elastic ring (b) that can be mapped from a line segment with length $\lambda_2\Gamma$. With increasing hydrostatic pressure, the shape of the cross section transforms from a circle to an ellipse, then to a peanut shape (c).

(10,10) CNT. It is almost a straight line within a small range of compression ratios. Of course, this is only a theoretical relationship curve. As shown in Sec. IV, buckling occurs when the pressure reaches a critical value.

IV. STRUCTURAL TRANSITIONS OF SINGLE-WALLED CARBON NANOTUBES UNDER HYDROSTATIC PRESSURE

In this section, we apply a mesh-free method to study the structural transitions of SWCNTs under hydrostatic pressure. In the study in Ref. 40, we developed a mesh-free method to model the buckling behavior of SWCNTs under axial compressing and twisting loadings. Under hydrostatic pressure, a SWCNT uniformly deforms along the axial direction, and we only need to consider the deformation of a cross section. Thus, the problem is similar to that of an elastic ring [Fig. 9(b)]. However, the interactions between the radial deformation, the uniform axial deformation, and the possible twisting deformation should also be considered. This ring can be mapped directly from a line segment in the reference configuration [Fig. 9(a)], and this line segment has a width of $\lambda_2\Gamma$ [here, we use Fig. 1(c) as the reference configuration and the cell structure in Fig. 1(c) as the image of all of the cell structures]. The deformation relative to the undeformed SWCNT can be expressed in terms of the displacements u_2 and u_3 and λ_2 and Θ. The gradient components F_{22}, G_{222}, F_{32}, and G_{322} can be calculated with u_2 and u_3, and the other gradient components are determined by λ_1 and Θ. Thus, the strain energy density is a function of F_{22}, G_{222}, F_{32}, G_{322}, λ_1, and Θ. The stable configurations of the system are identified with the minimization of the total energy,

$$E=\int_{B_0} W(F_{22},G_{222},F_{32},G_{322},\lambda_1,\Theta)dS\int_{B_0} u_N p dS. \quad (18)$$

In the mesh-free simulation, a series of nodes is collocated on the line segment (they can also be viewed as being on the undeformed ring). The displacement relative to the undeformed ring is approximated as

$$\begin{bmatrix} u_2 \\ u_3 \end{bmatrix} = \sum_{i=1}^{N} \phi_i \begin{bmatrix} u_{2i} \\ u_{3i} \end{bmatrix}, \quad (19)$$

where ϕ_i is the mesh-free shape function that is defined on the one-dimensional line segment, u_{2i} and u_{3i} are the nodal parameters, and N is the number of nodes which supporting domain cover the evaluated point.[30–35] The deformation gradients are approximated as

$$F_{22}=\bar{F}_{22}+\sum_{i=1}^{N}\phi_{i,2}u_{2i}, \quad G_{222}=\bar{G}_{222}+\sum_{i=1}^{N}\phi_{i,22}u_{2i},$$

$$F_{32}=\bar{F}_{32}+\sum_{i=1}^{N}\phi_{i,2}u_{3i}, \quad G_{322}=\bar{G}_{322}+\sum_{i=1}^{N}\phi_{i,22}u_{3i}, \quad (20)$$

where $\bar{F}_{22}$, $\bar{G}_{222}$, $\bar{F}_{32}$, and $\bar{G}_{322}$ are the gradients of the undeformed ring and can be calculated exactly; $\phi_{i,2}$ and $\phi_{i,22}$ are, respectively, the first- and second-order derivatives of ϕ_i with respect to X_2.

Assuming that N nodes are used, the total unknown vector can be written as

$$\mathbf{U}=(u_{21},u_{31},\ldots,u_{2i},u_{3i},\ldots,u_{2N},u_{3N},\lambda_1,\Theta)^T. \quad (21)$$

The nonequilibrium force and the stiffness matrix can be calculated as

$$\mathbf{f}=\frac{\partial E}{\partial \mathbf{U}}, \quad \mathbf{K}=\frac{\partial^2 E}{\partial \mathbf{U}^2}. \quad (22)$$

The equilibrium configurations can be obtained by iteratively solving $\mathbf{K}\Delta\mathbf{U}=\mathbf{f}$ until $\mathbf{f}$ reaches zero. It should be noted that $\mathbf{K}$ may not be positive-definite around the buckling (structural transition). A simple way to overcome this difficulty is to replace $\mathbf{K}$ with $\mathbf{K}+\alpha\mathbf{I}$, where $\mathbf{I}$ is the identity matrix, and α is a positive number that is slightly larger than the magnitude of the most negative eigenvalue of $\mathbf{K}$.[38]

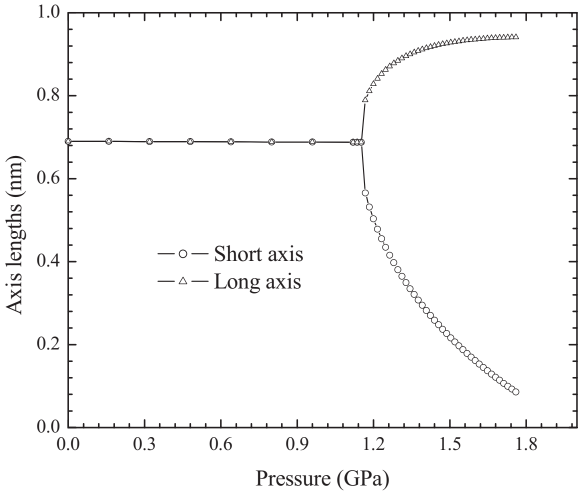

FIG. 10. Variation of lengths of the long and short axes with pressure for (10,10) CNT.

Numerical simulation is first carried out for the (10,10) SWCNT. The computation reveals that the first structural transition occurs when the pressure reaches 1.168 GPa, and the cross section of the tube transforms from a circle to an ellipse [Fig. 9(c)]. With the increasing pressure, the length of the long axis increases, but the short axis reduces its length. At about a pressure of 1.3 GPa, the second structural transition occurs, and the cross section of the tube transforms from an elliptical to a peanut shape [Fig. 9(c)]. When the pressure further increases, the short axis continues to reduce its length, but the length of the long axis remains almost unchanged. Figure 9(c) shows the configuration transformations of the cross section at several pressure values. Figure 10 shows the variation of the long and short axes with the pressure (prior to the first structural transition, the cross section is a circle, and the two axes have the same lengths). To reveal the dependence of the critical pressure of the first structural transition on the chirality and radius of the CNTs, the computations are performed for $(n,0)$, (n,n), and $(3n,2n)$ CNTs with different radii. Figure 11 plots the variation of the first transition pressure with the tube radius for $(n,0)$, (n,n), and $(3n,2n)$ CNTs. It is found that the first transition pressure has no obvious dependence on the chirality of the CNTs.

V. CONCLUDING REMARKS

The mechanical properties of SWCNTs are studied in the scheme of the higher-order gradient continuum. The effect of the second-order deformation gradient is considered in the approximation of the deformations of the microscale bond vectors, and the continuum elastic potential is obtained by equating the deformation energy of a representative cell with that of an equivalent volume of the continuum. Thus, the continuum constitutive model can be established. The deformation map from a graphite sheet to an undeformed CNT is set in an appropriate form with three geometrical parameters, and the structural and elastic properties can be obtained with the minimization of the cell structure. The response of the CNTs under the axis-symmetrical loadings can be computed by changing the values of the three geometrical parameters. Computations reveal that the elastic properties of CNTs have a dependence on the chirality and the tube radius, but when the tube radius is larger than 0.5 nm, the axial and circumferential elastic properties of CNTs are pretty close to those of the graphite sheet, and the maximum error is less than 2%. Therefore, CNTs can be viewed as a hollow cylinder with a minor thickness, and the elastic properties at the tangent directs are almost the same with the graphite sheet.

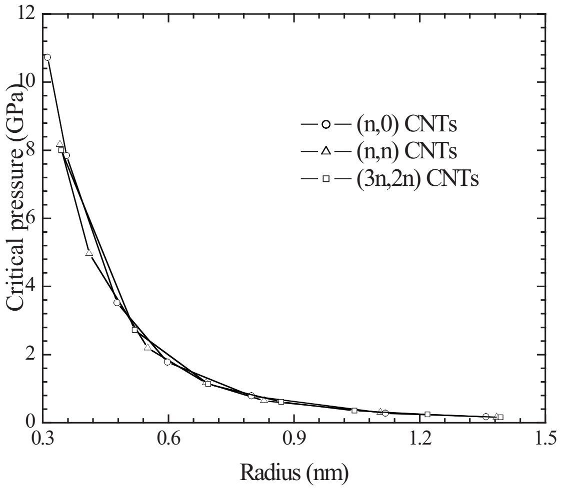

FIG. 11. Critical pressure of the first structural transition versus tube radius for $(n,0)$, (n,n), and $(3n,2n)$ CNTs.

Under hydrostatic pressure, CNTs deform uniformly along the axial direction, and a SWCNT can be simplified as an elastic ring. The strain energy of CNTs can be written in terms of the radial displacement of the ring and the two geometrical parameters corresponding to the axial and twisting deformations. The mesh-free method is used to determine a stable configuration in the scheme of the higher-order gradient continuum. The pressure-induced structural transitions are studied for different chiralities of CNTs. It is found that the chirality of CNTs has a slight effect on the critical transition pressure.

ACKNOWLEDGMENTS

The work described in this paper was fully supported by the City University of Hong Kong Strategic Research Grant (Project No. 7002204). The work was also supported by the computing facilities provided by ACIM.

[1] S. Iijima, Nature (London) **354**, 56 (1991).
[2] B. I. Yakobson, C. J. Brabec, and J. Bernholc, Phys. Rev. Lett. **76**, 2511 (1996).
[3] T. Belytschko, S. P. Xiao, G. C. Schatz, and R. S. Ruoff, Phys. Rev. B **65**, 235430 (2002).
[4] K. M. Liew, C. H. Wong, X. Q. He, M. J. Tan, and S. A. Meguid, Phys. Rev. B **69**, 115429 (2004).
[5] K. M. Liew, X. Q. He, and C. H. Wong, Acta Mater. **52**, 2521 (2004).
[6] K. M. Liew, C. H. Wong, X. Q. He, and M. J. Tan, Phys. Rev. B **71**, 075424 (2005).
[7] S. Govindjee and J. L. Sackman, Solid State Commun. **110**, 227 (1999).
[8] K. M. Liew and Q. Wang, Int. J. Eng. Sci. **45**, 227 (2007).
[9] C. Q. Ru, J. Mech. Phys. Solids **49**, 1265 (2001).
[10] Q. Wang and K. M. Liew, Phys. Lett. A **363**, 236 (2007).
[11] C. Y. Li and T. W. Chou, Phys. Rev. B **69**, 073401 (2004).
[12] X. Q. He, S. Kitipornchai, and K. M. Liew, J. Mech. Phys. Solids **53**, 303 (2005).
[13] L. F. Wang and H. Y. Hu, Phys. Rev. B **71**, 195412 (2005).
[14] K. M. Liew, Y. Hu, and X. Q. He, J. Comput. Theor. Nanosci. **5**, 581 (2008).
[15] J. H. Weiner, *Statistical Mechanics of Elasticity* (Wiley, New York, 1983).
[16] E. B. Tadmor, G. S. Smith, N. Bernstein, and E. Kaxiras, Phys. Rev. B **59**, 235 (1999).
[17] E. B. Tadmor, M. Ortiz, and R. Phillips, Philos. Mag. A **73**, 1529 (1996).
[18] V. B. Shenoy, R. Miller, E. B. Tadmor, D. Rodney, R. Phillips, and M. Ortiz, J. Mech. Phys. Solids **47**, 611 (1999).
[19] P. Zhang, Y. Huang, P. H. Geubelle, P. A. Klein, and K. C. Hwang, Int. J. Solids Struct. **39**, 3893 (2002).
[20] P. Zhang, H. Jiang, Y. Huang, P. H. Geubelle, and K. C. Hwang, J. Mech. Phys. Solids **52**, 977 (2004).
[21] M. Arroyo and T. Belytschko, Phys. Rev. B **69**, 115415 (2004).
[22] M. Arroyo and T. Belytschko, Int. J. Numer. Methods Eng. **59**, 419 (2004).
[23] P. Sunyk and P. Steinmann, Int. J. Solids Struct. **40**, 6877 (2003).
[24] X. Guo, J. B. Wang, and H. W. Zhang, Int. J. Solids Struct. **43**, 1276 (2006).
[25] J. B. Wang, X. Guo, H. W. Zhang, L. Wang, and J. B. Liao, Phys. Rev. B **73**, 115428 (2006).
[26] R. D. Mindlin, Int. J. Solids Struct. **1**, 417 (1965).
[27] D. Y. Sun, D. J. Shu, M. Ji, F. Liu, M. Wang, and X. G. Gong, Phys. Rev. B **70**, 165417 (2004).
[28] P. Tangney, R. B. Capaz, C. D. Spataru, M. L. Cohen, and S. G. Louie, Nano Lett. **5**, 2268 (2005).
[29] J. A. Elliott, J. K. W. Sandler, A. H. Windle, R. J. Young, and M. S. P. Shaffer, Phys. Rev. Lett. **92**, 095501 (2004).
[30] T. Belytschko, Y. Krongauz, D. Organ, M. Fleming, and P. Krysl, Comput. Methods Appl. Mech. Eng. **139**, 3 (1996).
[31] Z. Tang, S. Shen, and S. N. Atluri, Comput. Model. Eng. Sci. **4**, 177 (2004).
[32] J. Ren, K. M. Liew, and S. A. Meguid, Int. J. Mech. Sci. **44**, 2393 (2002).
[33] K. M. Liew, Y. Q. Huang, and J. N. Reddy, Int. J. Numer. Methods Eng. **56**, 2331 (2003).
[34] K. M. Liew, X. L. Chen, and J. N. Reddy, Comput. Methods Appl. Mech. Eng. **193**, 205 (2004).
[35] K. M. Liew, L. X. Peng, and S. Kitipornchai, Comput. Methods Appl. Mech. Eng. **196**, 2358 (2007).
[36] J. Tersoff, Phys. Rev. B **37**, 6991 (1988).
[37] D. W. Brenner, Phys. Rev. B **42**, 9458 (1990).
[38] J. E. Dennis and R. B. Schnabel, *Numerical Methods for Unconstrained Optimization and Nonlinear Equations* (Prentice-Hall, Englewood Cliffs, NJ, 1983).
[39] H. Jiang, P. Zhang, B. Liu, Y. Huang, P. H. Geubelle, H. Gao, and K. C. Hwang, Comput. Mater. Sci. **28**, 429 (2003).
[40] Y. Z. Sun and K. M. Liew, Comput. Mater. Sci. **43**, 444 (2008).